Journal of Photochemistry & Photobiology, A: Chemistry 469 (2025) 116525

Contents lists available at ScienceDirect

Journal of Photochemistry & Photobiology, A: Chemistry

journal homepage: www.elsevier.com/locate/jphotochem

A doubly protonated fluorescent dye for acid-base measurement

S.A. Stock [a], R. Firouzihaji [a], M. Hantro [b], M.E. Kleybolte [c], B. Truglia [a], C. van Dyck [b], S. Vagin [d], D. Lazzari [a,e], J. Tuszynski [a], A. Meldrum [a,*]

[a] Department of Physics, University of Alberta, Edmonton, AB T6G 2E1, Canada
[b] Department of Physics, Université de Mons, 20 place du Parc, Mons 7000, Belgium
[c] Wacker Chair of Macromolecular Chemistry, Technical University of Munich, Lichtenbergstraße 4, 85747 Garching bei München, Germany
[d] Heinz Maier-Leibnitz Zentrum (MLZ), Technical University of Munich, Lichtenbergstraße 1, 85748 Garching bei München, Germany
[e] DIMEAS, Politecnico di Torino, Corso Duca degli Abruzzi 24, Turin I-10129, Italy

ARTICLE INFO

Keywords:
Luminescence
Fluorescence
Base
Protonation
Equilibrium
Sensor dye

ABSTRACT

Commonly employed pH-sensing dyes include coumarins, rhodamines, fluoresceins, and cyanines, each offering distinct spectral properties and tunability. The design of fluorescent acid-base sensors typically involves organic dye molecules with functional groups that can interact with OH^- ions. Here, we demonstrate a distyrylbenzene-based fluorescent base-sensing dye (double-protonated carboxy-functionalized 1,4-bis(4-pyridyl-2-vinyl)benzene; c-P4VB·2HX, where X = Cl but can also be other anions) that provides a larger color change and a wider range of base concentrations due to the two-step deprotonation, compared to any previously-reported fluorescent base sensors. The c-P4VB·2HCl is orange luminescent in its doubly protonated state, which evolves through yellow, greenish, and finally electric blue in its unprotonated state, with fluorescence quantum efficiencies typically higher than 50 %. The c-P4VB·2HCl and its unprotonated form (c-P4VB) are highly soluble in moderately polar solvents like (short-chained) alcohols, dimethyl sulfoxide, and dimethyl formamide, and modestly soluble in water, due to the combination of pyridine groups and the caproic acid functional group. The reaction equilibria for the two deprotonation stages were investigated, the effect of the added OH^- concentration and ambient temperature on the emission color and spectra were quantified, and biological imaging was finally demonstrated.

1. Introduction

The detection of OH^- is important for industrial chemical processes, water treatment, agriculture, biomedical monitoring, drug discovery, and electrochemical systems [1,2,3]. In this regard, optical detection methods have many benefits: they are non-invasive, enable continuous monitoring, are resistant to environmental interference, and do not require frequent recalibration [4]. Standard litmus papers represent a widely known OH^- indicator that relies on a visual comparison of color patches with respect to a reference standard. While inexpensive and useful, such indicators provide only a rough estimate of OH^- concentration and suffer from a number of other long-understood limitations [5,6]. Perhaps most importantly for this work, the ten to fifteen different dye variants commonly used in litmus paper (often including amino-orcein or hydroxyorcein) are colorimetric as opposed to fluorescent, which limits their widespread use in many of the above-mentioned applications. Fluorescent dyes have several advantages for C(OH^-) (OH^- concentration) measurement, including a strong signal [4], the potential to be used for imaging applications [7], relatively easy integration into fiber-optic sensors [8], and superior quantification as compared to that achievable with colorimetric dyes [4,9,10]. In particular, fluorescence color-change dyes are especially suitable for sensing applications as compared to those employing quenching alone, because they enable ratiometric measurements that sidestep issues with photobleaching or other environmental parameters that cause unwanted emission intensity fluctuations.

The majority of available fluorescent pH indicators, specifically, concentrate on the acidic or neutral region of the pH scale, including fluorescein [11], rhodamine–naphthalimide conjugates [12], 1-amino-perylene bisimides [13], or cyclohexandiamines [14]. Only a relatively few base-detecting fluorescent sensors have their response in the high C(OH^-) range. Perhaps one of the best-known is SNARF (seminaphthorhodafluor), a molecule first described as a fluorescence sensor in 1991 [15] and now available commercially as a base sensor [7].

* Corresponding author.
E-mail address: ameldrum@ualberta.ca (A. Meldrum).

https://doi.org/10.1016/j.jphotochem.2025.116525
Received 17 March 2025; Received in revised form 22 May 2025; Accepted 26 May 2025
Available online 29 May 2025

Several variants of SNARF have been developed with generally similar characteristics [16,17,18,19,20]. All SNARF derivatives feature a xanthene-like arrangement fused to a naphthofuran or naphthopyran ring, with a hydroxyl group attached to the naphthyl part of the molecule. The hydroxyl group plays a key role in the pH-sensitive fluorescence properties of the dye. SNARF can be deprotonated on this hydroxyl group yielding a dual-emission fluorescence spectrum with maxima at 583 nm and 631 nm. In increasingly basic environments the yellow emission decreases while the red fluorescence correspondingly increases. Demonstrations of the SNARF indicator dyes were limited to $< \sim 10^{-5}$ M OH^-. Other base-sensing fluorescent dyes like "CPIPA" [21], iminocoumarin derivatives [3], aza-BODIPYs [22], diketopyrrolopyrrole [23] and squarylium dyes [24], are based on quenching upon deprotonation, which reduces the fluorescence intensity. To avoid the above-mentioned inaccuracies associated with intensity-based sensors, another reference dye is commonly added [3,22,23,] which complicates the measurement and often suffers from differential photobleaching.

This work reports on an acid-base sensor with the widest fluorescence spectral shift reported to date. We use a deprotonation reaction that takes place in doubly-protonated 1,4-bis(4-pyridyl-2-vinyl)benzene derivative (c-P4VB·2HX, X = Cl or potentially other anions; see Scheme 1 and Fig. 1), a chromophore whose unprotonated neopentyl-substituted version was recently designed as a widely tunable laser dye [25]. The two protonation sites located at terminal positions of the main conjugated backbone are (nearly) equivalent and stem from sterically accessible 4-pyridyl groups. The lead structure of c-P4VB·2HX has been synthesized a few times in the literature but generally with short-chain sidegroups (*i.e.*, methoxy groups) and thus has limited solubility in organic solvents [26,27]. For c-P4VB·2HX (hereafter we will refer to c-P4VB as simply "B", and the ionized double protonated c-P4VB·$2H^{2+}$ as H_2B^{2+}), the presence of OH^- in solution leads to a double-deprotonation and a large fluorescence color shift from orange to electric-blue. We quantify the spectra, develop a simple equilibrium model, measure the fluorescence in a variety of solvents and temperatures, and investigate the OH^- sensing and biological imaging capability of this fluorescent dye. The molecule shows several advantageous properties over commercially available SNARF dyes, including a much larger emission wavelength shift, which leads to improved sensitivity and operation to a higher C(OH^-) range than achievable previously.

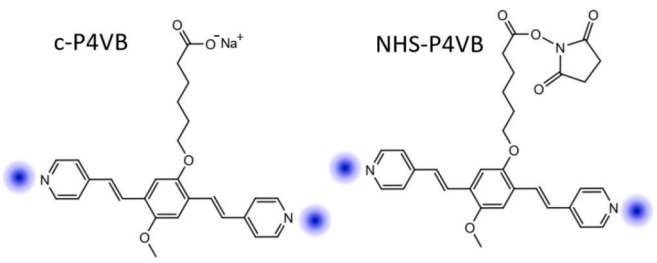

Fig. 1. Schematics of the structures of c-P4VB (left) and NHS-P4VB (right). The protonation sites are illustrated by the shaded blue circles. (For interpretation of the references to color in this figure legend, the reader is referred to the web version of this article.)

2. Methods

2.1. Synthesis of P4VB

The synthesis of c-P4VB (B) was modified from a previously reported procedure [25,28] (see Scheme 1), employing a multi-step process starting from commercially available 4-methoxyphenol (**1**). In the first step 4-methoxyphenol (**1**) was alkylated via Williamson ether synthesis with 6-bromohexanoic acid (**2**). After isolation, 6-(4-methoxyphenoxy) hexanoic acid (**3**) was converted into 6-(2,5-bis-(bromomethyl)-4-methoxyphenoxy)hexanoic acid (**4**) via a Blanc-type bromo-methylation using paraformaldehyde and HBr. Subsequently, the corresponding diphosphonate (**5**) was prepared by reacting **4** with triethyl phosphite under elevated temperatures. Finally, c-P4VB was obtained via a Horner-Wadsworth-Emmons reaction by stirring the diphosphonate **5** with 2 equivalents of 4-pyridinecarbaldehyde (**6**) in the presence of potassium *tert*-butoxide in dry *tert*-butanol. The fine yellow powder was then dissolved in anhydrous EtOH (5 mM) and an aqueous concentrated HCl was added to reach 15 mM solution in order to ensure full protonation. The EtOH was then evaporated at room temperature under ambient conditions and the c-P4VB·2HCl was obtained as red fibrous microcrystals. Some of the c-P4VB was then reacted with N-hydroxysuccinimide in presence of a carbodiimide reagent EDC (1-ethyl-3-(3-dimethylaminopropyl)carbodiimide hydrochloride) and triethylamine in dry THF. For this, 200 mg (0.43 mmol) of c-P4VB, 170 mg (0.88

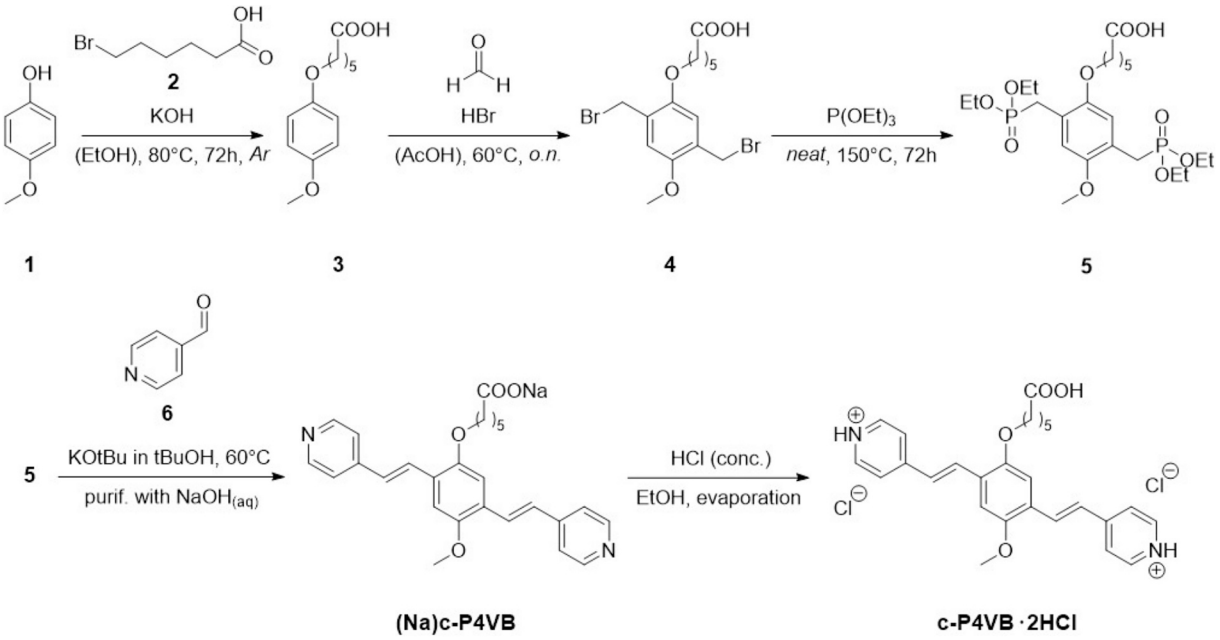

Scheme 1. Synthesis steps for c-P4VB·2HCl.

mmol) EDC, 100 mg (0.86 mmol) NHS and 91 mg (0.90 mmol) triethylamine were mixed in 10 ml of tetrahydrofuran (taken from an MBRAUN solvent purification system) and stirred vigorously overnight, resulting in a fine yellow suspension. This was taken into a syringe and filtered through a PTFE syringe filter (0.45 μm). The filtrate was evaporated to dryness, the resulting solid was washed quickly but thoroughly with water and collected by suction filtration. After drying under vacuum, 198 mg (85 %) of yellow-orange NHS-P4VB were obtained.

2.2. Fluorescence measurement

Fluorescence spectroscopy was done using an intensity- and wavelength-calibrated miniature fiber-optic spectrometer. The pump beam came from a continuous wave UV-optimized Ar^+ ion laser with emission lines at 352 and 364 nm and a power of 2 mW. Time resolved photoluminescence (TRPL) employed an Alphalas Picopower 375-nm pulsed laser (~20 ps pulses) operated at 5 MHz. A Becker-Hickl HPM-100 single-photon-counting detector and associated photon counting module were used to register the decay statistics. Fluorescence imaging of the as-produced crystals was done on a Nikon TE2000 fluorescence microscope utilizing a 365-nm excitation LED and a 409-nm dichroic filter. Fluorescence images of the liquid samples was performed using a Sony a6400 consumer camera with the samples standing under a 365-nm UV lamp. Both JPG and ARW images were captured in order to ensure that the image coloring and compression algorithm would not significantly affect the results (ARW is a raw image format). For absorption spectroscopy, we used a Thorlabs fiber-coupled stabilized deuterium UV light source connected to another miniature fiber-optic spectrometer, using an identical cuvette with plain EtOH as the reference. Cell cultures were imaged using a Zeiss 710 confocal microscope (Carl Zeiss AG) with the excitation was at 405 nm and emission wavelengths were recorded in approximately 4 nm intervals between 450 and 600 nm. The absolute quantum efficiencies were measured with a customized integrating sphere. Samples were placed in quartz cuvettes, inserted into the integrating sphere, and excited with a 365-nm LED using a narrowpass filter to eliminate possible overlap with the emitted fluorescence. The dye samples were compared against blank solvent by finding the relative differences in the number of incident 365-nm photons and those emitted from the sample in order to calculate the AQY.

2.3. Density functional theory

To investigate the effect of protonation on the electronic structure of c-P4VB, five selected molecular configurations (illustrated in Fig. S3) were simulated using Gaussian 16 software [29]. Because of the two pyridine groups and one carboxylic group on c-P4VB, there are actually three centers in the molecule capable of acid-base interactions. The proton at the carboxylic group is more strongly bound compared to the pyridines and does not affect the spectral properties of the chromophore [30]. Thus, we refer hereafter to the singly- and doubly-protonated states as referring to the pyridines only. The fully deprotonated structure is depicted in Fig. S3(a), while the protonation sites are illustrated in Fig. S3(b–e). All calculations for these states were performed using density functional theory (DFT). The CAM-B3LY0P [31] exchange–correlation hybrid functional was employed in combination with the 6–31++G(d,p) Gaussian basis set. Solvent effects were accounted for using the implicit polarizable continuum model (PCM) [32] with ethanol as the solvent. Excited state properties were modelled using time-dependent DFT (TD-DFT). Optimized geometries for both the ground and excited states were obtained using the tight convergence criteria specified in Gaussian 16. Vibrational frequencies were calculated to confirm convergence of the optimized geometries. A table of geometries and frequencies re provided in the SI.

2.4. Fluorescent labeling

In order to demonstrate a simple application, A549 human lung carcinoma cell lines were cultured and labeled with NHS-P4VB *in vitro*. NHS-P4VB was first dissolved in dimethyl sulfoxide (DMSO) to a concentration of 10 μM. Cells were cultured in T75 flasks until reaching approximately 80 % confluency. They were then subcultured into glass-bottomed cell culture dishes after an initial wash with a phosphate-buffered saline (PBS) to remove debris and non-adherent cells. After aspirating the PBS, 2 mL of TrypLE™ Express Enzyme 1X (Gibco, ThermoFisher Scientific) was added to enzymatically dissociate the cells. To facilitate detachment, the flask was incubated at 37 °C for a few minutes. Once trypsinization was complete, fresh medium was added at a 4:1 ratio to neutralize the enzyme. Cells were then counted using a hemocytometer, and a density of 6×10^5 cells per dish was used for plating. Following seeding, cells were incubated overnight at 37 °C with 5 % CO_2 to promote adhesion. The cell culture medium was then removed and replaced with fresh DMEM containing NHS-P4VB at a different final concentration of 100 nM. Samples were then incubated under standard conditions (37 °C, 5 % CO_2) for 15 min. Following incubation, the medium was aspirated, and cells were washed twice with 1 mL of PBS. Fresh DMEM medium (without NHS-P4VB) was then added, and samples were incubated for an additional two hours to allow stabilization before confocal microscopy analysis.

3. Results and discussion

The c-P4VB·2HCl (B·2HCl) forms thin needle-like crystals ranging from ~5 to 100 μm in length (Fig. 2). ^{1}H NMR spectra (Fig. S1) were consistent with the molecular structures in Fig. 1. The dye appears as an orange powder that emits a bright red fluorescence when illuminated with a 365-nm LED. The deprotonated form appears as a yellow powder consisting of similarly elongated prismatic crystals with green fluorescence (Fig. 2). The B·2HCl is highly soluble in ethanol (EtOH) and other alcohols such as butanol and octanol, as well as other mildly polar organic solvents including organic carbonates, and it is modestly soluble in water. The NHS-P4VB was not initially protonated and it appeared as

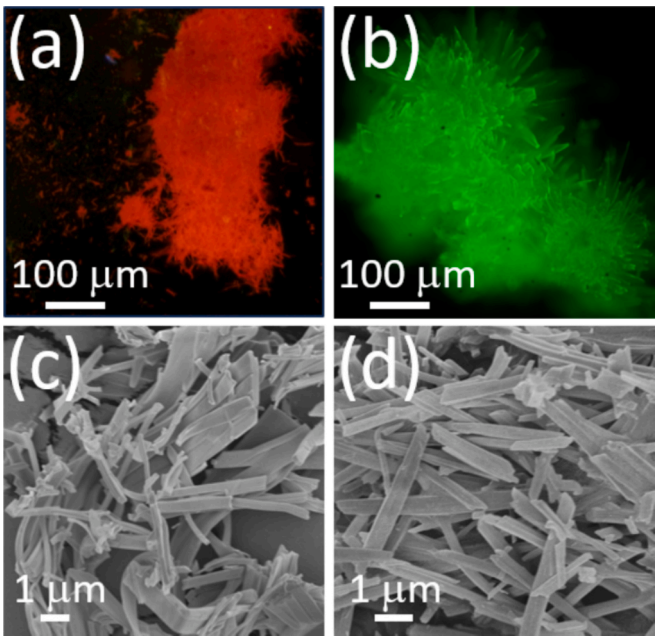

Fig. 2. (a) Fluorescence image of c-P4VB·2HCl crystallized from EtOH. (b) Precursor unprotonated c-P4VB crystallized from EtOH. (c,d) Secondary electron images showing the extended prismatic crystals for the c-P4VB·2HCl and c-P4VB, respectively.

similar prismatic green-fluorescent microcrystals as for the c-P4VB shown in Fig. 2.

When dissolved in EtOH, the H_2B^{2+} shows strong S_0 to S_1 and S_0 to S_2 absorption peaks at 456 and 357 nm, respectively, and it emits orange fluorescence maximized at 584 nm (Fig. 3) with an absolute quantum efficiency (AQE) of 47 %. The absorption and fluorescence of H_2B^{2+} changed drastically upon deprotonation with KOH. The absorbance peaks blueshifted to 403 and 331 nm, respectively, while the fluorescence maximized at 490 nm and the AQE was 74 %. We found a significant range in the AQE measurements (±18 % maximum) for samples taken at different times from days to months after the initial synthesis, but with no clear time-dependent trend. The reason for this is probably a combination of factors including the sensitivity of the AQE measurement to small changes in the experimental setup [33] and sample-to-sample variability. The mean fluorescence lifetimes fit well to a weighted biexponential decay, with mean amplitude lifetimes decreasing from 2.53 ± 0.29 ns in the doubly protonated state (with initial concentration of 250 μM) to 2.41 ± 0.17 and 2.34 ± 0.04 ns in presence of 50 and 200 μM KOH, respectively (Fig. 3), where the latter 1σ errors are derived from the uncertainties in the fitting parameters. When viewed under a UV lamp, the fluorescence clearly evolved from a bright orange through yellow, pale green, and finally to electric blue upon increasing concentrations of KOH (Fig. 2(c) – where the term "electric blue" was made by visual comparison to standard color charts). The corresponding emission spectra for the full set of samples are provided in Fig. S4.

The fluorescence shifts monotonically from orange to blue with increasing $C(OH^-)$ (Fig. 3(c)). The two sequential pyridine deprotonatation reactions associated with this color shift are given by:

$$H_2B^{2+} + OH^- \rightleftharpoons HB^+ + H_2O \quad (1a)$$

$$HB^+ + OH^- \rightleftharpoons B + H_2O \quad (1b)$$

The concentrations of the three dye species in Eq. (1) were estimated by fitting the absorbance data to a pair of Gaussians for each protonation state (Fig. 4). The original doubly-protonated dye (H_2B^{2+}) has two absorbance peaks: S_0 to S_2 at 357.1 ± 0.3 and S_0 to S_1 at 456.7 ± 0.3 nm, while the unprotonated dye has absorbances centered at 328.9 ± 0.1 and 403.4 ± 0.1 nm, respectively. The means and standard deviations of the unprotonated c-P4VB (=B) and H_2B^{2+} (doubly protonated) states were then fixed and a mid-range KOH concentration (250 μM, greenish solution in Fig. 3(c)) was used to fit the absorbance maxima relating to HB^+. The reported maxima are in good agreement with the DFT results (Tables 1 and 2), which show the same blueshift as a function of deprotonation. All the absorbance peak centers and standard deviations were then fixed and the rest of the absorbance spectra were fit accordingly by allowing only the intensity prefactors to vary. We finally assumed that the H_2B^{2+}, HB^+, and B concentrations are proportional to the area under the absorbance spectra, which allows one to extract the estimated concentration of all three states for any OH^- concentration. This method is supported by the DFT results, which showed virtually the same absorption oscillator strength for all of the pyridine protonation states (Table 1).

In order to better understand the dynamics and equilibrium of this double-deprotonation reaction, an equilibrium model was developed to describe the system and compare the calculated concentrations of the doubly-, singly-, and unprotonated species with experimentally-estimated values. The equilibrium concentrations of the doubly protonated state $[H_2B^{2+}]$, the singly protonated species $[HB^+]$, the unprotonated species [B], hydroxide ions $[OH^-]$, and water $[H_2O]$ are denoted as such in the following expressions. The equilibrium constants k_1 and k_2 for the first and second deprotonation reactions are given by:

$$k_1 = \frac{[HB^+][H_2O]}{[H_2B^{2+}][OH^-]} \quad (2a)$$

$$k_2 = \frac{[HB][H_2O]}{[HB^+][OH^-]} \quad (2b)$$

Moreover, several mass balance equations must hold for these reactions, given the initial dye concentration, $C(H_2B^{2+})_0$ and the initial concentration of OH^- added to the solution $C(OH^-)_0$, according to:

$$[OH^-] = C(OH^-)_0 - ([HB^+] + [B]) \quad (3a)$$

$$[H_2O] = [HB^+] + [B] \quad (3b)$$

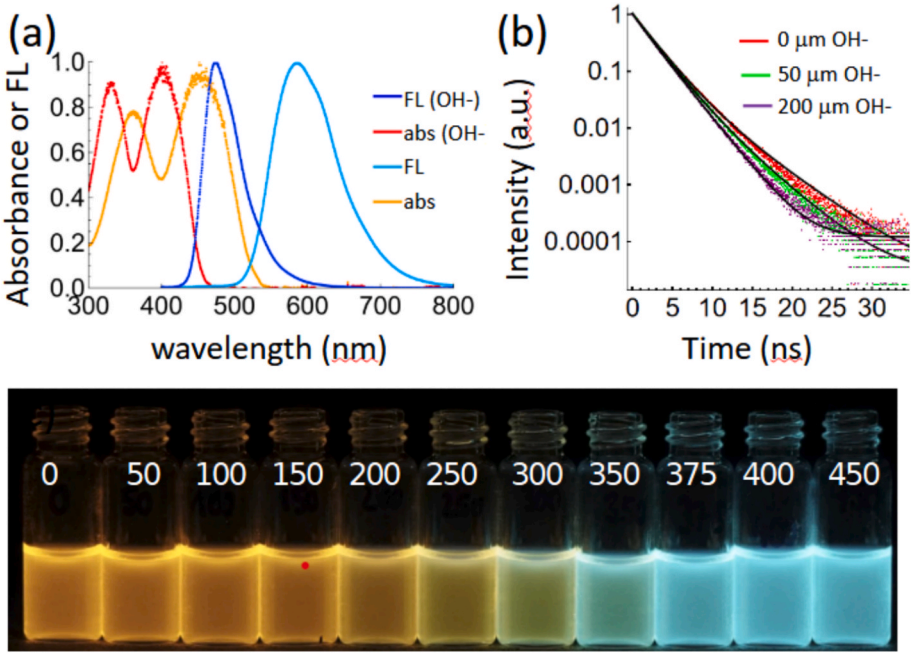

Fig. 3. (a) Normalized fluorescence and absorbance spectra of B·2HCl solutions (in EtOH) taken under UV illumination with an Ar^+ ion laser. Fully deprotonated samples are indicated by (OH^-) in the legend; (b) Fluorescence decays for 100 μM B·2HCl in EtOH with different concentrations of KOH (OH^-) with the bi-exponential fits denoted by black lines; The image at the bottom is a photograph of a set of 11 vials with varying concentrations of OH^- (from KOH, in μM) as shown. The concentration of B·2HCl was 250 μM in EtOH, in all 11 vials.

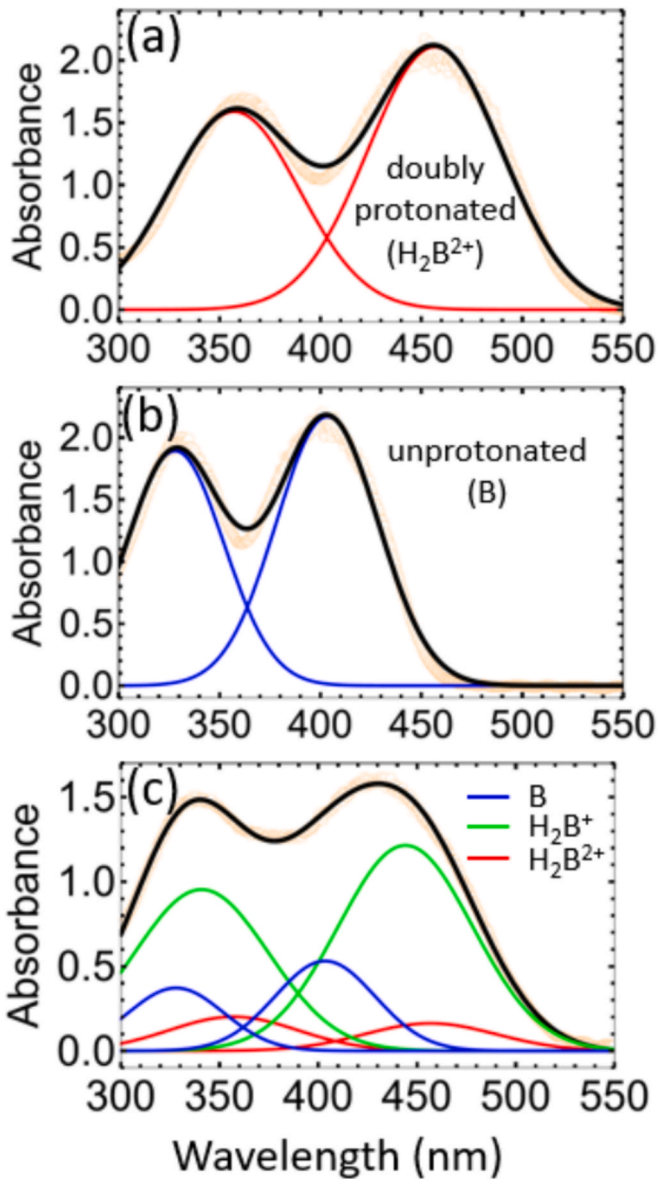

Fig. 4. (a) Absorbance spectrum for H_2B^{2+}, and the associated double-Gaussian fit. (b) The same as in (a), but for the deprotonated c-P4VB (B). (c) Absorbance spectrum and associated multi-Gaussian fit for the sample with 250 μM KOH.

Table 1
Calculated spectral properties of the various protonation states: total energies (E_{tot}), emission wavelength (λ_{em}) with corresponding oscillator strengths (f_{em}), absorption wavelengths ($\lambda_{|,|1}$ and $\lambda_{|,|2}$) with corresponding oscillator strengths ($f_{|,|1}$ and $f_{|,|2}$).

	λ_{em}(nm)	f_{em}	$\lambda_{|,|1}$(nm)	$f_{|,|1}$	$\lambda_{|,|2}$(nm)	$f_{|,|2}$
Pristine	520	1.79	389	1.36	305	0.44
1-proton left	583	1.69	439	1.27	334	0.45
1-proton right	581	1.67	438	1.25	332	0.46
2-protons	608	1.62	459	1.27	346	0.61

$$C(H_2B^{2+})_0 = [H_2B^{2+}] + [HB^+] + [B] \quad (3c)$$

Rearranging these expressions to solve for $[H_2B^{2+}]$, $[HB^+]$, and [B], one obtains the following set of coupled equations:

Table 2
Calculated (DFT) and experimental transition wavelengths for c-P4VB·$2H^{2+}$, c-P4VB·H^+, and c-P4VB. The mean values represent the average of the right- and left-protonated states (see the Supporting Information).

	H_2B^{2+} (S_1) (nm)	H_2B^{2+} (S_0) (nm)	HB^+ (S_0) (nm)	HB^+ (S_1) (nm)	B (S_0) (nm)	B (S_1) (nm)
Measured	357.1 ± 0.3	456.7 ± 0.3	340.9 ± 15.8	444.1 ± 3.6	328.9 ± 0.1	403.4 ± 0.1
DFT	346	459	333 (mean)	438.5 (mean)	305	389.5

$$[H_2B^{2+}] = \frac{[H_2B^{2+}]_0}{1 + \frac{k_1[OH^-]}{[H_2O]} + \frac{k_1k_2[OH^-]^2}{[H_2O]^2}} \quad (4a)$$

$$[HB^+] = \frac{k_1 \cdot [H_2B^{2+}] \cdot [OH^-]}{[H_2O]} \quad (4b)$$

$$[B] = \frac{k_1k_2 \cdot [H_2B^{2+}] \cdot [OH^-]^2}{[H_2O]^2} \quad (4c)$$

These equations were numerically fit to the concentration data with a dynamic solver written in Mathematica to obtain $[H_2B^{2+}]$, $[HB^+]$, and [B], (the concentrations of doubly-, singly- and un-protonated dye as a function of the initial $C(OH^-$- effectively, the concentration of KOH added). In addition, we included a free "background water" term, $C(H_2O)_0$, in the calculations in case of any water initially present in the (nominally) anhydrous EtOH used in the experiments. The latter is trivially achieved by letting $[H_2O] = [HB^+] + [B] + C(H_2O)_0$ in Eqs. (3) and (4). To fit the model results to the estimated concentrations of the three dye species, the two equilibrium constants and $C(H_2O)_0$ were chosen as the fitting variables.

The resulting data and model fit show reasonable agreement considering the uncertainties in the experimental concentration calculations (Table 3; Fig. 5(a)). The model captures the general trends of all three species. Several conclusions can be drawn from this result: first, the equilibrium constant is higher for the first deprotonation than it is for the second one ($k_1 = 138$ *vs.* $k_2 = 7$) but the two processes still cannot be treated independently. Second, the best-fit initial water concentration, $C(H_2O)_0$, turned out to be zero. This was considered surprising; although nominally anhydrous EtOH was used in the experiments and the container was carefully sealed when not in use, some humidity is accumulated during the experiments. This suggests either that the water builds up quite slowly or its effect is masked by the uncertainties in the measurements. Third, the fully protonated H_2B^{2+} (initially 250 μM) was nearly completely used up by the time ~300 μM of KOH was added to the solution. One may also note that the fit for the singly-protonated state (Fig. 5(a), green curve) is fairly poor at high $C(OH^-)$; this is likely because the fitting of the absorbance data is less reliable when there is very little HB^+ present (note that the HB^+ is the only protonation state whose absorbance cannot be isolated and fit independently).

As previously mentioned, fluorescence is more practical than absorbance for sensing applications. Ideally, for base-sensing one wants to track the emission color shift as a function of OH^- present in the solution, like in Fig. 3(c). To demonstrate the base-sensing capability of c-P4VB·2HCl (equivalently, H_2B^{2+}) in the simplest manner and without requiring specialized equipment, we analyzed the red and blue color channels from photos of the fluorescent vials taken with a consumer camera, with the initial idea that H_2B^{2+} would contribute to the red channel and B to the blue one. One might then assume the ratio of the blue and red image intensities given by the signal $S = I_B/I_R$ is simply proportional to $[B]/[H_2B^{2+}]$ (*i.e.* the ratio of unprotonated to fully protonated dye) from Eqs. (4a) and (4c). However, several additional factors must be considered when modeling the color in the images. First, the blue and red channels have overlap as can be clearly seen when

Table 3
Model concentrations (in micromolar) of c-P4VB·2HCl, c-P4VB·HCl, and c-P4VB as a function of C(KOH) in an anhydrous EtOH solution.

$C(OH^-)$	0	50	100	150	200	250	300	350	375	400	450
$\mathbf{H_2B^{2+}}$	250	200	150	101	54	16	3	1	2	1	0
$\mathbf{HB^+}$	0	49	97	139	170	159	101	67	57	50	39
B	0	1	3	9	26	75	146	182	192	200	211

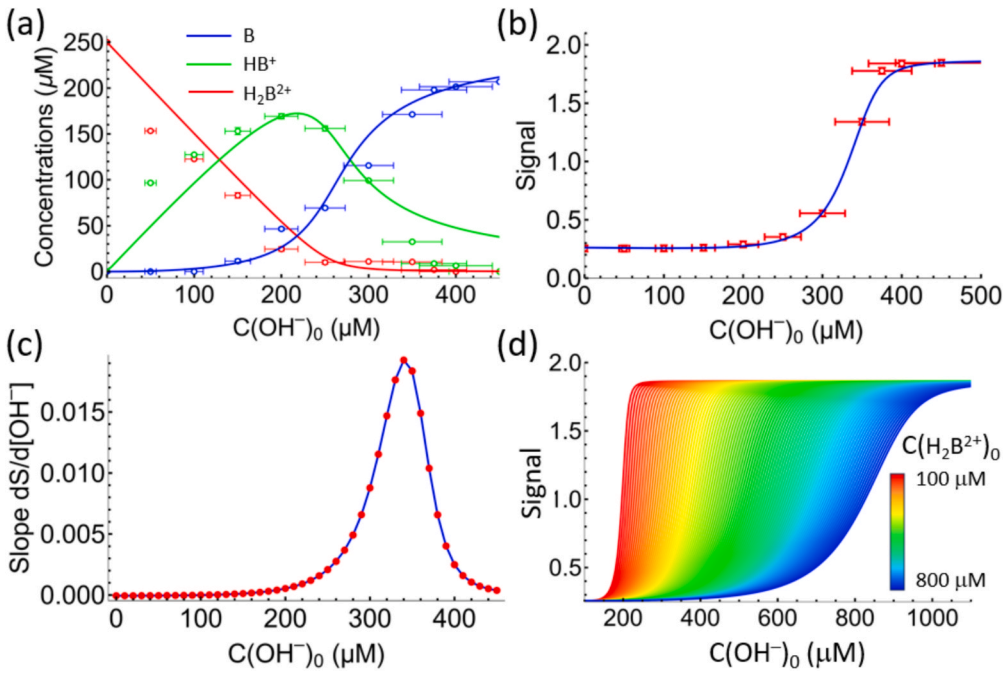

Fig. 5. (a) Calculated concentrations [H_2B^{2+}], [HB^+], and [B] as a function of the amount of hydroxide added to the solution, along with the associated model fits from Eq. 4(a-c). The fitting parameters were $k_1 = 138$, $k_2 = 7$, and $C(H_2O)_0 = 0$. (b) The signal $S = I_B / I_R$ from the fluorescent vials imaged in Fig. 2(c) and the corresponding model fit (Eq. (5). The fit parameters were A = 1.24, $b = 0.346$, $c = 0.609$, $C = -0.172$, and $D = 107$ μM. The vertical error bars come from the uncertainties in the Gaussian fits and are much smaller (similar in size to the data points) than the (horizontal) dilution errors. (c) The slope (sensitivity) of the signal model in (b). (d) The effect on the modeled signal curve of increasing the initial dye concentration $C(H_2B^{2+})_0$ from 100 to 800 μM. As the dye concentration increases, the curve shifts to become sensitive to higher and wider range of solution $C(OH^-)$.

comparing the fluorescence spectra to the transmission data for the Sony Bayer filter (Fig. S9). Moreover, the width of the emission spectra will further cause some of the red emission to appear in the blue channel and vice-versa. Second, there is inevitably a vertical offset representing the ratio of the background signals (in comparison to the pure [B]/[H_2B^{2+}] ratio) in the channel ratio data that must be incorporated into the response function. Finally, and somewhat more subtly, the camera response to small initial changes in the concentrations of the fluorescent dye species was noticeably different from the spectrometer response to the absorbance changes. While the absorbance and fluorescence spectra changed fairly significantly at certain wavelengths (Figs. S8 and S10), the color seen in the fluorescence images was almost the same at lower C (OH^-) (Fig. 3(c)). Thus, we included a delay factor in the response function to account for this sensing difference. Incorporating these modifications, the final equation to model the observed I_B/I_R ratio in the fluorescence images like those in Fig. 3(c) is:

$$S = B/R = A\frac{[B] + b\cdot[H_2B^{2+}]}{[H_2B^{2+}] + c\cdot[B]} + C \tag{5}$$

where b and c account for the amount of overlap in the blue and red channels, C is the ratio offset, and A is a scaling parameter. The delay factor, D, is incorporated via a modification to Eq. 3(a) according to $[OH^-] = (C(OH^-)_0 - D) - ([HB^+] + [B])$, which is substituted into Eq. (5) though its common dependencies on [H_2B^{2+}] and [B] (Eq. 4).

The resulting numerical fit, with A, b, c, C, and D as the fitting parameters acceptably tracks the signal $S = I_B/I_R$ ratios from the cuvette images (Fig. 4(b)). The signal response in the images is a sigmoidal function with an initially negligible slope that becomes steep in the region between approximately 300 and 400 μM $C(OH^-)$ and maximizes at 340 μM, where the slope was computed by finding the derivative dS/dC (OH^-) using the central difference formula (Fig. 5(c)). The uncertainties in the signal, δS, were found by finding the standard deviation from five different samples at the same $C(OH^-)$ concentration, which turned out to be proportionally smaller than the volume dilution errors, $\delta C(OH^-)$, which are shown as horizontal error bars. If we treat the smallest detectable change as being equal to $3\delta S/m$, where m is the slope of the response function, then at the optimum concentration the smallest detectable change on $C(OH^-)$ is 1.36 μM for the fluorescence images taken with a Sony a6400 consumer camera.

As one can see from the signal curve in Fig. 5(b), the sensitivity at low concentrations is essentially zero. This is because the fluorescence changes are very small at low $C(OH^-)$. However, if we simply examine the fluorescence spectra (Fig. S4), take the ratio of the wavelengths $\lambda_{500}/\lambda_{590}$ as the signal, linearly interpolate between 0 and 50 μM $C(OH^-)$ to find the sensitivity, and linearize the data to find $3\sigma_{noise}$, then the lowest detectable base concentration becomes 4.3 μM and the smallest detectable change is 7.9 nM at the peak of the sensitivity. Clearly, the limit of detection and the smallest detectable change in $C(OH^-)$ is dependent on the measurement method; moreover, because of the sigmoidal response function it is optimum at intermediate OH^- concentrations and poorest at low concentrations.

Next, the effect of the ambient temperature on the fluorescence was investigated. Initially, we supposed that deprotonation might be preferred at higher temperatures. The results in Fig. 6 clearly support this idea, where, for all C(OH^-) concentrations the fluorescence shifted toward shorter wavelengths as the temperature increased from 21 °C to 90 °C. This experiment used butanol as the solvent because of its higher boiling point; however, a similar trend can be observed in EtOH at lower temperatures (20–40 °C) (see the Supporting Information). As can be seen by a comparison to Fig. 4, the signal reached a higher value than would have been expected for 250 μM C(OH^-) – in fact, the signal is so high that there is insufficient OH^- present in the solution to produce it. Even without any base present, the sample in butanol evolved a blue fluorescence indicating almost complete thermally-induced deprotonation at 90 °C (Fig. 6). This was fully reversible upon cooling the sample back to room temperature.

One can find a rough estimate of the protonation energy simply by examining the fluorescence. The fluorescence spectrum of the H_2B^{2+} at 50° (without added KOH) most closely resembled the room-temperature 150-μM KOH sample in Fig. 3(c), which has concentrations of 101, 139, and 9 μM for [H_2B^{2+}], [HB^+], and [B], respectively, according to the model Fig. 5. If we assume that the same concentrations are obtained by dissociation upon heating in the absence of KOH, then according to the reactions $H_2B^{2+} \rightleftharpoons HB^+ + H^+$ and $HB^+ \rightleftharpoons B + H^+$ the dissociation constants, *k*, with the above concentrations are 7.7 x 10^{-5} and 3.6 × 10^{-6} μM for the first and second deprotonations, and from $\Delta G^\circ = -RT \cdot ln(k)$ one obtains corresponding Gibb's free energy changes ΔG°, of 25.4 and 33.6 kJ/mol. The positive free energy (and comparatively high effective pKa) means that the reactants are favored in the deprotonation reaction. In other words, the proton "sticks" quite well to the binding sites on the dye, and deprotonates quite little in an acid-neutral BuOH solvent. These correspond to an effective binding energy of 0.26 eV and 0.35 eV and a pK_a of 4.1 and 5.4 for the two deprotonations, respectively, in butanolic solutions. The calculated pK_a of 5.4 is, perhaps coincidentally, close to pKa for pyridine in water of 5.2–5.3, as listed in numerous chemical databases. The effective binding energy is lower than one would expect for a covalent protonation of the nitrogen atoms, in agreement with the donor–acceptor bond character, and also possibly because of solvent interactions like solvation or charge stabilization. Despite the roughness of these estimates, which comes only from the fluorescence, the values obtained are comparable to those for the protonation of similar dyes (*e.g.*, [34]).

The structure of c-P4VB is related to that of the diarylethenes and especially to the distyrylbenzenes [35,36]. The diarylethenes represent a large class of photochromic dyes [37,38,39] that are of interest because of their use as photochromic switches [40], typically involving reversible open *vs.* closed-ring bonding reconfiguration [41] and corresponding visible color change upon exposure to light. Some of these compounds are known to be photochemically reactive, undergoing a photoinduced cis–trans isomerization, and also to show solvatochromism [42]. An advantage of the diarylethenes is their excellent photochemical stability. Interestingly, P4VB can be seen as a derivative of these structures that fortuitously maintains the excellent stability under prolonged irradiation, but instead of photochemical switching it undergoes a double-protonation reaction with an extremely large change in the fluorescence emission wavelengths. Both the fully protonated and unprotonated form (H_2B^{2+} and B) were quite photostable. Exposing solutions to UV light at up to 250 mW/cm^2 for up to one hour did not cause any noticeable decrease or change in the luminescence. The c-P4VB does show a positive solvatochromism, with its emission peak shifting monotonically from 480 to 495 nm on going from water to EtOH to toluene (see the Supporting Information).

The optical characterization described above was done in EtOH or BuOH because both forms of the dye (protonated vs. unprotonated) have a high solubility. To illustrate more common potential applications of c-P4VB, we next functionalized to c-P4VB with N-hydroxysuccinimide (NHS) as shown in the experimental section. We then performed simple color tests for 5 mM NHS-c-P4VB dye in aqueous HEPES buffer solution (pH 6.8). In water, both forms of the dye (unprotonated vs. protonated) were sensitive to the additions of acid or base but with a large concentration delay, consistent with the buffering action of the solution (Fig. 7). Thus we conclude that, although the solubility limit was in the range of 50–100 μM, P4VB can work in aqueous solutions, which should permit the development of several possible applications.

To demonstrate one such application, a set of A549 cell cultures were labeled with unprotonated NHS-c-P4VB, using methods described in the experimental section. We found that the NHS-c-P4VB appeared to preferentially labeled the nuclear region at or around the nuclear envelope and slightly inside the nucleus also with the characteristic electric blue color of P4VB (Fig. 7(c)). For a direct comparison, we show similar images taken with mitotracker red dye (see the Supporting Information). Images taken at 479 nm and 576 nm emission wavelengths showed that, indeed, the dye is much brighter at the shorter wavelength, consistent with only a low level of protonation. This clearly shows that NHS-c-P4VB has applications as a dye for biological imaging including protonation/deprotonation effects of ligands on intracellular structures. We imagined that information on intracellular pH might be obtained by examining the ratio of the intensities in the 479 and 576 nm images, as shown in Fig. 7(e). Indeed, while the interpretations at this stage are tenuous, we observe that the background level is just slightly but uniformly and consistently higher outside the nuclei than inside, which would indicate a very slightly lower pH in the cytosol. This initial result would be consistent with the pH gradient observed across the nuclear membrane of mammalian cells [43] and suggests that P4VB could illuminate the nuclear pH, which is typically assumed to simply be the same as it is in the cytosol [44].

Given that it is possible to dissolve the NHS-functionalized version of

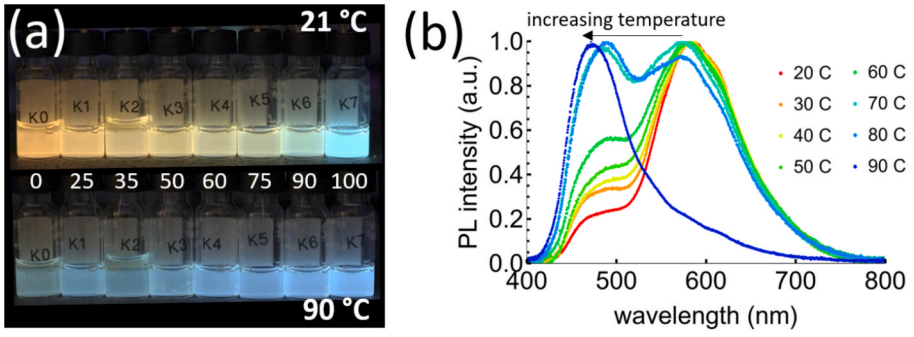

Fig. 6. (a) Photographs of a set of samples with 100 μM [H_2B^{2+}] in butanol taken at temperatures of 21 and 90 °C, respectively. The added KOH concentrations in μM for each vial are shown in white across the middle. (b) The corresponding fluorescence spectra of the sample without any KOH added (the leftmost vial in the images) over the entire set of temperatures. The fluorescence shifted from red-orange (red line) to blue as the temperature increased from 20 to 90 °C, indicating increasing deprotonation with increasing temperature. (For interpretation of the references to color in this figure legend, the reader is referred to the web version of this article.)

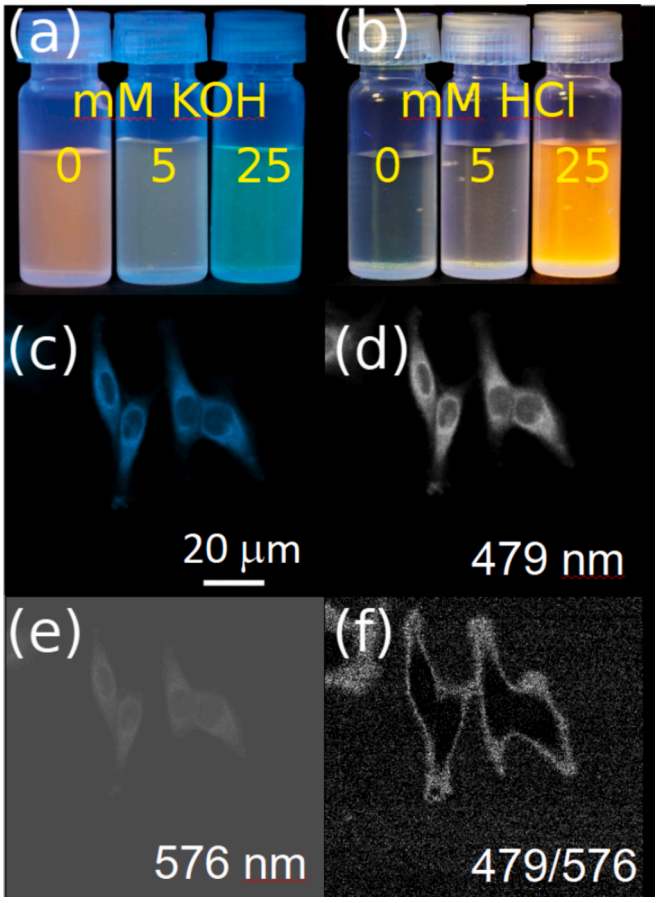

Fig. 7. Color changes for protonated (a) and unprotonated (b) NHS-functionalized cP4VB in HEPES buffer solution. The corresponding fluorescence spectra are shown in the Supporting Information. (c) Confocal microscopy images of NHS-c-P4VB-labeled A549 cancer cells with nuclei in the centre and actin filaments surrounding them. The cells exhibit increased elongation due to the presence of stress fibers formed along the lines connecting adhesion points to the cover slip surface. (d) 479 nm emission image; (e) 576 nm emission image; (f) ratio image. Images have been contrast enhanced for viewing (the 576 nm emission image would otherwise appear completely dark on the page).

the dye in aqueous buffer, we next attempted to find the pK_a values for the two protonations for this situation as well, via titration of HCl (measured with a pH meter) into the aqueous buffer combined with absorbance and fluorescence spectroscopy. Unfortunately, it was quite difficult to perform the multi-Gaussian fitting on the absorbance data in this case due to the lower solubility than for the previous situation, which caused the absorbance spectra to be weak and noisy; however, fortuitously we found that the singly protonated fluorescence was in this case nearly completely quenched (see the corresponding spectra in the Supporting Information). In other words, the unprotonated electric blue fluorescence decreased to nearly zero with decreasing pH, and then the double-protonated orange fluorescence increased as the measured pH decreased further. This type of behavior is well-documented in certain polyprotic weak bases like 2,2′ bipyridine [45], carnosine (with three widely-separated pK_a values) [46], and phenanthroline [47] Thus, we could treat the protonation reactions sequentially as a first approximation, in which the blue-emitting unprotonated dye initially converted to a nearly quenched singly-protonated state before the orange-emissive, doubly-protonated one could be observed. Measuring the pH with a pH meter and modeling the two cases independently with the Hill equation [48,49,50] leads to $pK_{a1} = 6.3$ and $pK_{a2} = 4.3$ in aqueous buffer (note that the pKa symbols are reversed from earlier, since this represents protonation rather than deprotonation). This means the first proton "sticks" more strongly than the second one does in aqueous solutions. Of course there are also uncertainties in the experiment and the assumptions used to extract the pK_a values, but they appear not unreasonable for the protonation of the pyridine groups.

We finally comment on the advantages and limitations of B and H_2B^{2+} as a fluorescent acid-base sensor. Obviously, one limitation is that sensing must be done at a known temperature for which the dye has been calibrated. This is likely a common issue for most, if not all, deprotonation-based fluorescent sensors, although this issue has been little discussed in the sensing literature. Second, the double-deprotonation of the pyridine groups makes it much more difficult to model the equilibrium dynamics than would be the case for a single reaction. Isobestic points, for example, are not readily observable due to the simultaneous existence of the two pyridine-related protonation states. Moreover, the singly protonated state, c-P4VB·HCl, is impossible to isolate and its effects on the fluorescence and absorption are masked by the c-P4VB·2HCl and c-P4VB species. Finally, the sensitivity to small changes in $C(OH^-)$ is weakest near a concentration of zero, which limits the minimum base concentration that can be detected.

Despite these limitations, however, there are several important advantages offered by c-P4VB·2HCl compared to the relatively few previous fluorescent base sensors. First, the two-step reaction enables operation to higher $C(OH^-)$, as long as other factors such as dye concentration are equivalent. The relatively large sensing range found in practice is likely due, in part, to the double de-protonation requirement which requires at least twice as much OH^- to complete it, in comparison to the more common single-protonated dyes. Like SNARF, it utilizes the ratiometric method, which is well understood to give a significant advantage over fluorescence-quenching-based sensing. The fluorescence shift from orange to electric blue is also larger than that for any other fluorescent base sensor, to the best of our knowledge. These factors also improve the minimum detectable change in $C(OH^-)$ and the limit of detection, although this is dependent on the measurement method. The ratio method is, moreover, insensitive to any potential photobleaching, which was negligible in the present case anyway. We found it to be soluble in diethyl sulfoxide (even mixed with buffer), which is commonly used for cell labeling and imaging. Finally, the synthesis is quite simple and can it be applied to aqueous solvents and biological imaging.

4. Conclusions

This work reported on a base sensor that has, to our knowledge, the widest fluorescence spectral shift reported to date. Sensing was obtained via a double de-protonation reaction that takes place on two nearly equivalent highly-accessible pyridine groups situated at each end of the molecule. The absorption peaks for the doubly and unprotonated dye were determined by measurement, while the singly-protonated state absorption spectrum could not be isolated and had to be estimated by multiple peak fitting. The results agreed well with DFT calculations of the molecular energy levels. To obtain the relevant sensing parameters such as the equilibrium constants and binding energies, the equilibrium reactions were solved numerically and compared to the experimental estimates of the concentrations of the three different dye protonation states as a function of the OH^- concentration. In addition to showing a large fluorescence color shift, c-P4VB·2HCl works up to higher $C(OH^-)$ than previous fluorescent dyes that could be found in the literature, at similar dye concentrations. Images taken with a simple consumer camera could be used to quickly estimate the concentrations of the various dye species present, and the amount of a strong base in ethanolic solutions could be directly obtained from fluorescence images or spectra. While considerable improvement can be obtained by using spectroscopic data, the ease of measurement using simple photographic imaging suggests that c-P4VB·2HCl might be useful for a variety of practical base-sensing applications including fluorescence imaging of cells.

5. Author Statement*

S. Stock and R Firouzihaji did most of the experiments. M. Hantro and C. Van Dyck did the DFT. M Kelybolte and S Vagin made the materials and contributed intellectually. D. Lazzari, B. Truglia and J. Tuszynski did the cell labeling. A. Meldrum conceptualized it and wrote most of the MS.

CRediT authorship contribution statement

S.A. Stock: Investigation. **R. Firouzihaji:** Investigation. **M. Hantro:** Formal analysis. **M.E. Kleybolte:** Methodology. **B. Truglia:** Methodology. **C. van Dyck:** Methodology. **S. Vagin:** Methodology. **D. Lazzari:** Methodology. **J. Tuszynski:** Methodology. **A. Meldrum:** Writing – review & editing, Writing – original draft, Supervision, Conceptualization.

Declaration of competing interest

The authors declare that they have no known competing financial interests or personal relationships that could have appeared to influence the work reported in this paper.

Acknowledgments

The authors gratefully acknowledge support from the Natural Sciences and Engineering Research Council of Canada, the Alberta Innovates Advance Program, and the MITACs Globalink program. We acknowledge use of equipment in the Collaborative Ultrafast Spectroscopy Laboratory (CUSL) for Materials and Device Characterization, which is generously funded by the Province of Alberta (Alberta Jobs, Economy, and Innovation Small Equipment Grant Program, RCP-22-024-SEG) and the Canada Foundation for Innovation John R. Evans Leaders Fund (CFI-JELF 42139). M.H. and C.V.D acknowledge the CECI (Consortium des Équipements de Calcul Intensif) for providing computation time and the support of Actions de Recherche Concertées (Project No. ARC-21/25 UMONS2). The authors thank two anonymous reviewers for thoughtful comments.

Appendix A. Supplementary data

Supplementary data to this article can be found online at https://doi.org/10.1016/j.jphotochem.2025.116525.

Data availability

Data will be made available on request.

References

[1] C.R. Schroder, B.M. Weidgans, I. Klimant, pH fluorosensors for use in marine systems, Analyst 130 (2005) 907–916.
[2] J.M. Price, W. Xu, J.N. Demas, B.A. DeGraff, Polymer-supported pH sensors based on hydrophobically bound luminescent ruthenium(II) complexes, Anal. Chem., 70 (1998) 265–270.
[3] A.S. Vasylevska, A.A. Karasyov, S.M. Borisov, C. Krause, Novel coumarin-based fluorescent pH indicators, probes and membranes covering a broad pH range, Anal. Bioanal. Chem., 387 (2007) 2131–2141.
[4] D. Wencel, T. Abel, C. McDonagh, Optical chemical pH sensors, Anal. Chem., 86 (2014) 15–29.
[5] J. Brennan, Potential sources of error using pH strips, sciencing.com, 2022.
[6] G.S. Walpole, The use of litmus paper as a quantitative indicator of reaction, Biochem. J 7 (1913) 260–267.
[7] R.C. Hunter, T.J. Beveridge, Application of a pH-sensitive fluoroprobe (C-SNARF-4) for pH microenvironment analysis in Pseudomonas aeruginosa biofilms, Appl. Environ. Microbiol. 71 (2005) 2501–2510.
[8] O.S. Wolfbeis, Fiber-optic chemical sensors and biosensors, Anal. Chem. 78 (2006) 3859–3874.
[9] J.R. Lakowicz, Principles of Fluorescence Spectroscopy, third ed., Springer Science, New York, 2010.
[10] F. Baldini, A.N. Chester, J. Homola, S. Martellucci, Optical Chemical Sensors, IOS Press, Amsterdam, 2006.
[11] M.M. Martin, L. Lindqvist, The pH dependence of fluorescein fluorescence, J. Lumin., 10 (1975) 381–390.
[12] Q.-J. Ma, H.-P. Li, F. Yang, J. Zhang, X.-F. Wu, Y. Bai, X.-F. Li, A fluorescent sensor for low pH values based on a covalently immobilized rhodamine–napthalimide conjugate, Sens. Actuat., B 166–167 (2012) 68–74.
[13] D. Aigner, S.M. Borisov, P. Petritsch, I. Klimant, Novel near infra-red fluorescent pH sensors based on 1-aminoperylene bisimides covalently grafted onto poly (acryloylmorpholine), Chem. Commun. (Camb.) 49 (2013) 2139–2141.
[14] J.-M. Zen, G. Patonay, Near-infrared fluorescence probe for pH determination, Anal. Chem., 63 (1991) 2934–2938.
[15] J.E. Whitaker, R.P. Haugland, F.G. Prendergast, Spectral and photophysical studies of benzo[c]xanthene dyes Dual emission pH sensors, Anal. Biochem., 194 (1991) 330–344.
[16] E. Nakata, Y. Nazumi, Y. Yukimachi, Y. Uto, H. Maezawa, T. Hashimoto, Y. Okamoto, H. Hori, Synthesis and photophysical properties of new SNARF derivatives as dual emission pH sensors, Bioorg. Med. Chem. Lett., 21 (2011) 1663–1666.
[17] C.S. Owen, P. Carango, S. Grammer, S. Bobyock, D.P. Leeper, pH-dependent intracellular quenching of the indicator carboxy-SNARF, J. Fluoresc. 2 (1992) 76–80.
[18] N. Marcotte, A.M. Brouwer, Carboxy SNARF-4F as a fluorescent pH probe for ensemble and fluorescence correlation spectroscopies, J. Phys. Chem. B 109 (2005) 11819–11828.
[19] M. Yassine, J.-M. Salmon, J. Vigo, P. Viallet, C-SNARF-1 as a pHi fluoroprobe: Discrepancies between conventional and intracellular data do not result from protein interactions, J. Photochem. Photobiol., B 37 (1997) 18–25.
[20] Z. Xu, A. Rollins, R. Alcala, R.E. Marchant, A novel fiber-optic pH sensor incorporating carboxy SNAFL-2 and fluorescent wavelength-ratiometric detection, J. Biomed. Mater. Res. 39 (1998) 9–15.
[21] S. Derinkuyu, K. Ertekin, O. Oter, S. Denizalti, E. Cetinkaya, Fiber optic pH sensing with long wavelength excitable Schiff bases in the pH range of 7.0-12.0, Anal. Chim. Acta 588 (2007) 42–49.
[22] T. Jokic, S.M. Borisov, R. Saf, D.A. Nielsen, M. Kuhl, I. Klimant, Highly photostable near-infrared fluorescent pH indicators and sensors based on BF2-chelated tetraarylazadipyrromethene dyes, Anal. Chem., 84 (2012) 6723–6730.
[23] D. Aigner, B. Ungerbock, T. Mayr, R. Saf, I. Klimant, S.M. Borisov, Fluorescent materials for pH sensing and imaging based on novel 1,4-diketopyrrolo-[3,4-c] pyrrole dyesdaggerElectronic supplementary information (ESI) available: NMR and MS spectra, further sensor characteristics and sensor long-time performance. See DOI: 10.1039/c3tc31130aClick here for additional data file, J Mater Chem C Mater, 1 (2013) 5685-5693.
[24] J. Griffiths, J. Mama, pH-dependent absorption and Øuorescence spectra of hydroxyaryl-squarylium dyes, Dyes Pigm., 44 (2000) 9–17.
[25] S. Lane, S. Vagin, H. Wang, W.R. Heinz, W. Morrish, Y. Zhao, B. Rieger, A. Meldrum, Wide-gamut lasing from a single organic chromophore, Light Sci Appl 7 (2018) 101.
[26] E.M. Ebeid, R.M. Issa, M. Ghoneim, S.A. El-Daly, Emission Characteristics and Micellization of Cationic 1,4-Bis(P-pyridyl-2-viny1)benzene Laser Dye, J. Chem. Soc. Faraday Trans. I (82) (1986) 909–919.
[27] E.M. Ebeid, M.M.F. Sabry, S.A. el-Daly, 1,4-Bis (fl- Pyridyl-2-Vinyl) benzene (P2VB) and 2,5-distyryl-pyrazine (DSP) as blue laser dyes, Laser Chem. 5 (1985) 223-230.
[28] A.P. Kalra, B.B. Eakins, S.I. Vagin, H. Wang, S.D. Patel, P. Winter, M. Aminpour, J. D. Lewis, V. Rezania, K. Shankar, G.D. Scholes, J.A. Tuszynski, B. Rieger, A. Meldrum, A nanometric probe of the local proton concentration in microtubule-based biophysical systems, Nano Lett., 22 (2022) 517–523.
[29] M.J. Frisch, G.W. Trucks, H.B. Schlegel, G.E. Scuseria, M.A. Robb, J.R. Cheeseman, G. Scalmani, V. Barone, G.A. Petersson, H. Nakatsuji, X. Li, M. Caricato, A.V. Marenich, J. Bloino, B.G. Janesko, R. Gomperts, B. Mennucci, H.P. Hratchian, J.V. Ortiz, A.F. Izmaylov, J.L. Sonnenberg, Williams, F. Ding, F. Lipparini, F. Egidi, J. Goings, B. Peng, A. Petrone, T. Henderson, D. Ranasinghe, V.G. Zakrzewski, J. Gao, N. Rega, G. Zheng, W. Liang, M. Hada, M. Ehara, K. Toyota, R. Fukuda, J. Hasegawa, M. Ishida, T. Nakajima, Y. Honda, O. Kitao, H. Nakai, T. Vreven, K. Throssell, J.A. Montgomery Jr., J.E. Peralta, F. Ogliaro, M.J. Bearpark, J.J. Heyd, E.N. Brothers, K.N. Kudin, V.N. Staroverov, T.A. Keith, R. Kobayashi, J. Normand, K. Raghavachari, A.P. Rendell, J.C. Burant, S.S. Iyengar, J. Tomasi, M. Cossi, J.M. Millam, M. Klene, C. Adamo, R. Cammi, J.W. Ochterski, R.L. Martin, K. Morokuma, O. Farkas, J.B. Foresman, D.J. Fox, Gaussian 16 Rev. B.01, Wallingford, CT, 2016.
[30] P.D. Thungon, H. Wang, S.I. Vagin, C.V. Dyck, P. Goswami, B. Rieger, A. Meldrum, A fluorescent alcohol biosensor using a simple microPAD based detection scheme, Front. Sens. 3 (2022).
[31] T. Yanai, D.P. Tew, N.C. Handy, A new hybrid exchange–correlation functional using the Coulomb-attenuating method (CAM-B3LYP), Chem. Phys. Lett. 393 (2004) 51–57.
[32] G. Scalmani, M.J. Frisch, Continuous surface charge polarizable continuum models of solvation. I. General formalism, J. Chem. Phys. 132 (2010).
[33] S. Leyre, E. Coutino-Gonzalez, J.J. Joos, J. Ryckaert, Y. Meuret, D. Poelman, P. F. Smet, G. Durinck, J. Hofkens, G. Deconinck, P. Hanselaer, Absolute determination of photoluminescence quantum efficiency using an integrating sphere setup, Rev. Sci. Instrum. 85 (2014) 123115.
[34] CAS Database List 260-94-6, 2024.
[35] H. Detert, O. Sadovski, E. Sugiono, Acidochromism of C2-symmetrical aza-analogues of 1,4-distyrylbenzene, J. Phys. Org. Chem. 17 (2004) 1046–1050.
[36] V. Schmitt, S. Moschel, H. Detert, Diaryldistyrylpyrazines: Solvatochromic and Acidochromic Fluorophores, Eur. J. Org. Chem. 2013 (2013) 5655–5669.
[37] A. Towns, Diarylethene dyes, Phys. Sci. Rev. 5 (2020).

[38] Z. Li, C. He, Z. Lu, P. Li, Y.-P. Zhu, Recent progress in all-visible-light-triggered diarylethenes, Dyes Pigm. 182 (2020) 108623.
[39] M. Irie, T. Fukaminato, K. Matsuda, S. Kobatake, Photochromism of diarylethene molecules and crystals: memories, switches, and actuators, Chem. Rev. 114 (2014) 12174–12277.
[40] Q.-F. Li, L. Zhang, M. Shen, J.-T. Wang, L. Jin, Z. Wang, Photochromic diarylethene induced fluorescence switching materials constructed by non-covalent interactions, J. Mater. Chem. C 11 (2023) 12828–12847.
[41] K. Matsuda, M. Irie, Diarylethene as a photoswitching unit, J. Photochem. Photobiol. C: Photochem. Rev. 5 (2004) 169–182.
[42] M. Morimoto, Y. Takagi, K. Hioki, T. Nagasaka, H. Sotome, S. Ito, H. Miyasaka, M. Irie, A turn-on mode fluorescent diarylethene: Solvatochromism of fluorescence, Dyes Pigm. 153 (2018) 144–149.
[43] O. Seksek, J. Bolard, Nuclear pH gradient in mammalian cells revealed by laser microspectrofluorimetry, J. Cell Sci. 109 (1996) 257–262.
[44] A. Nakamura, S. Tsukiji, Ratiometric fluorescence imaging of nuclear pH in living cells using Hoechst-tagged fluorescein, Bioorg. Med. Chem. Lett. 27 (2017) 3127–3130.
[45] E.C. Constable, C.E. Housecroft, The early years of 2,2′-bipyridine—a ligand in its own lifetime, Molecules 24 (2019) 3951.
[46] M.J. Horvat, N. Sakac, D. Jakobovic, M. Sak-Bosnar, Analytical characterization and quantification of histidine dipeptides, carnosine and anserine by modeling of potentiometric titration data, Int. J. Electrochem. Sci. 10 (2015) 5787–5799.
[47] A. Assefa, R. Srinivasu, P. Shyamala, G. Rao, Shift in pK_a of 1,10-phenanthroline in TBAB and PEG-400 micellar media: A potentiometric study, Am. J. Anal. Chem. 9 (2018) 397–405.
[48] A. Wallace, J.K. Shen, Chapter 19 - Predicting pKa Values with continuous constant pH molecular dynamics, Methods Enzymol. 466 (2009) 455-475.
[49] Y. Xiao, X. Luo, M. Zhao, Z. Sun, X. Qian, Y. Yang, Modulating the pK_a values of Hill-Type pH probes for biorelevant acidic pH range, ACS Appl. Biomater. 4 (2020) 2097–2103.
[50] S. Shen, Y. Yang, X. Luo, X. Qian, Hill-type pH probes, Anal. Bioanal. Chem. 415 (2023) 3690–3702.